

A stochastic view of the 2020 Elazığ $M_w 6.8$ earthquake (Turkey)

Théa Ragon¹, Mark Simons¹, Quentin Bletery², Olivier Cavalié², Eric
Fielding³

¹Seismological Laboratory, California Institute of Technology, Pasadena, CA, USA.

²Université Côte d'Azur, IRD, CNRS, Observatoire de la Côte d'Azur, Géoazur, France.

³Jet Propulsion Laboratory, California Institute of Technology, Pasadena, CA, USA.

Key Points:

- We infer a stochastic model for the distribution of subsurface fault slip associated with the 2020 Elazığ earthquake
- We account for uncertainties in both the depth-dependence of the assumed elastic structure and the location and geometry of the fault
- Our models are characterized by two primary patches of fault slip where distribution appears to be controlled by geometrical complexities

Corresponding author: Théa Ragon, tragon@caltech.edu

This article has been accepted for publication and undergone full peer review but has not been through the copyediting, typesetting, pagination and proofreading process, which may lead to differences between this version and the [Version of Record](#). Please cite this article as [doi: 10.1029/2020GL090704](https://doi.org/10.1029/2020GL090704).

This article is protected by copyright. All rights reserved.

15 **Abstract**

16 Until the M_w 6.8 Elazığ earthquake ruptured the central portion of the East Anatolian
 17 Fault (EAF, Turkey) on January 24, 2020, the region had only experienced moderate mag-
 18 nitude ($M_w < 6.2$) earthquakes over the last century. We use geodetic data to constrain
 19 a model of subsurface fault slip. We adopt an unregularized Bayesian sampling approach
 20 relying solely on physically justifiable prior information and account for uncertainties in
 21 both the assumed elastic structure and fault geometry. The rupture of the Elazığ earth-
 22 quake was mostly unilateral, with two primary disconnected regions of slip. This rup-
 23 ture pattern may be controlled by structural complexity. Both the Elazığ and 2010 M_w
 24 6.1 Kovancılar events ruptured portions of the central EAF that are believed to be cou-
 25 pled during interseismic periods, and the Palu segment is the last portion of the EAF
 26 showing a large fault slip deficit which has not yet ruptured in the last 145 years.

27 **Plain Language Summary**

28 The Elazığ earthquake ruptured the central portion of the East Anatolian Fault
 29 (EAF), a major strike-slip fault in eastern Turkey, on January 24, 2020. Before this event,
 30 the region had only experienced moderate magnitude earthquakes over the last century.
 31 We aim at understanding the rupture of this earthquake, and how it relates to the his-
 32 torical ruptures of the EAF. To do so, we use measurements of displacement at the sur-
 33 face to image the subsurface slip on the fault that occurred during the earthquake. As
 34 the characteristics of the crust are poorly known, we make realistic assumptions on the
 35 fault geometry and Earth structure, and build on novel approaches to account for the
 36 possible biases of our assumptions and to characterize the uncertainties of the imaged
 37 slip. We suggest that the Elazığ earthquake rupture may be controlled by structural com-
 38 plexity of the fault, and that two main regions of slip surround a fault bend acting as
 39 a barrier to rupture propagation. We also suggest that the fault segment located between
 40 Lake Hazar and the city of Palu is the last portion of the central EAF, showing a large
 41 deficit of the fault slip, which has not yet ruptured in the last 145 years.

42 **1 Introduction**

43 A large portion of Turkey is located on the Anatolian Plate (AP), which is slowly
 44 extruding westward as a result of the north-south collision between the Arabian and Eurasian
 45 tectonic plates (e.g., Mckenzie, 1970; McKenzie, 1972; McClusky et al., 2000). The west-

Accepted Article

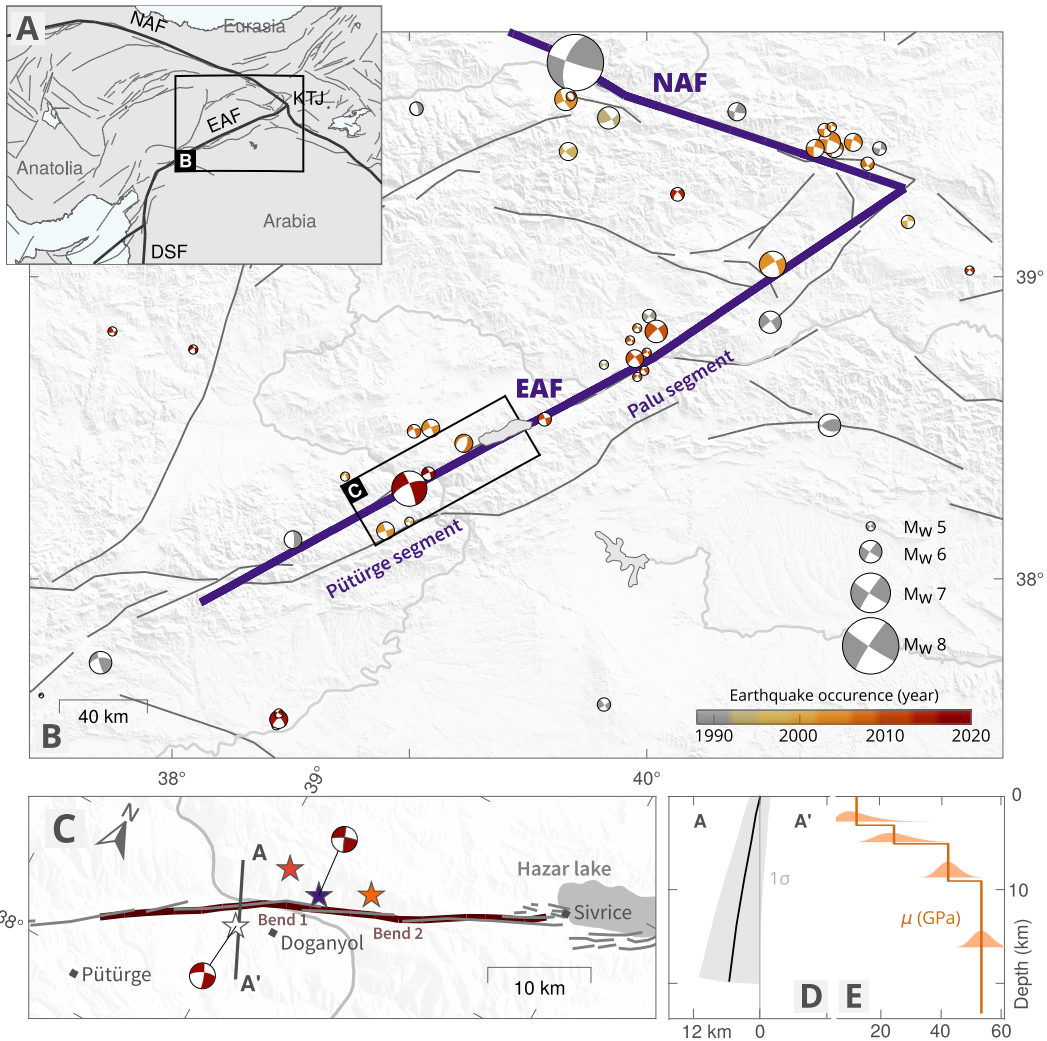


Figure 1. Tectonic setting and assumed characteristics for the Elazığ earthquake. (a) Tectonic setting of the area, plate boundaries are shown in thick black lines. East and North Anatolian Faults are labelled (EAF and NAF), as well as the Dead Sea fault (DSF) and Karlıova Triple Junction (KTJ). (b) Active fault traces (Basilic et al., 2013) and seismicity since 1976 (GCMT, Dziewonski et al., 1981) around the EAF and NAF. The Elazığ earthquake focal mechanism (GCMT) is in red. (c) Details of assumed (dark red) and mapped (gray) fault trace at the surface. Two structural bends of the causative fault geometry are highlighted. Possible epicenters are shown with white, red, purple and orange stars (from left to right on the map), respectively from GCMT, Jamalreyhani et al. (2020), KOERI and AFAD (2020). (d) Assumed fault geometry at depth and associated uncertainty (standard deviation of 5° around the assumed dip and 1 km around the fault surface trace). (e) Assumed shear moduli with depth (derived from Maden, 2012; Ozer et al., 2019) and associated uncertainties.

46 ward motion of the AP is predominantly accommodated along the North and East Anatolian faults (NAF and EAF, Fig. 1). The NAF experienced a sequence of destructive
47 earthquakes that struck within the last eighty years (e.g., A. Barka, 1996; Stein et al.,
48 1997; Armijo et al., 1999; Sengör et al., 2005). In contrast, the EAF is generally assumed
49 to be less active, and has only experienced small to moderate events over the last cen-
50 tury, although large ($M > 7$) earthquakes have occurred in the historical record (e.g., Am-
51 braseys, 1970; Ambraseys & Jackson, 1998; Hubert-Ferrari et al., 2020).

52
53 The EAF is a left-lateral 600-km-long strike-slip fault linking the Dead Sea fault
54 (DSF, Fig. 1) to the Karlıova Triple Junction (KTJ, Fig. 1) where it intersects with the
55 right-lateral NAF (e.g., Yilmaz et al., 2006; Duman & Emre, 2013). The EAF has a com-
56 plex geometry divided into several main segments, each of them characterized by bends,
57 pull-apart basins or compressional structures (e.g., Duman & Emre, 2013), and also com-
58 prises multiple secondary sub-parallel and seismically active structures delineating a 50-
59 km-wide fault zone (e.g., Bulut et al., 2012). The EAF accommodates a displacement of
60 9 to 15 mm/yr (Cetin et al., 2003; Reilinger et al., 2006; Cavalié & Jónsson, 2014; Ak-
61 tıg et al., 2016; Bletery et al., 2020), with creep dominantly at depths greater than 5
62 km (Cavalié & Jónsson, 2014; Bletery et al., 2020). As a comparison, the NAF shows
63 creep rates around 20-25 mm/yr below a locking depth of 7-25 km (e.g. Cakir et al., 2014a;
64 Hussain et al., 2018; Kaneko et al., 2013; Walters et al., 2011; Wright et al., 2001). Shal-
65 lower portions of the EAF are characterized by an highly varying inter-seismic slip deficit,
66 some portions being fully coupled while others appear to be at least partially creeping
67 (Bletery et al., 2020).

68 The January 24 2020 M_w 6.8 earthquake ruptured the EAF between the Hazar Pull-
69 apart Basin and the city of Pütürge (Fig. 1). In the area, the main fault has been mapped,
70 from the interpretation of aerial photos and field studies, as a sinuous trend interrupted
71 by bends and step-overs whose widths do not exceed a kilometer (Duman & Emre, 2013).
72 Coseismic surface rupture does not show a significant horizontal component and is prob-
73 ably mostly gravitational (Tatar et al., 2020). In this study, we investigate the subsur-
74 face rupture of the Elazığ earthquake and its relationship to fault geometry and inter-
75 seismic slip deficit. While assuming a fault structure with a realistic geometry, we also
76 account for its inherent uncertainties, as well as uncertainties related to assumptions on
77 the crustal structure. We adopt a Bayesian sampling approach which allows us to sam-
ple a large panel of possible slip models and to estimate the posterior uncertainty on the

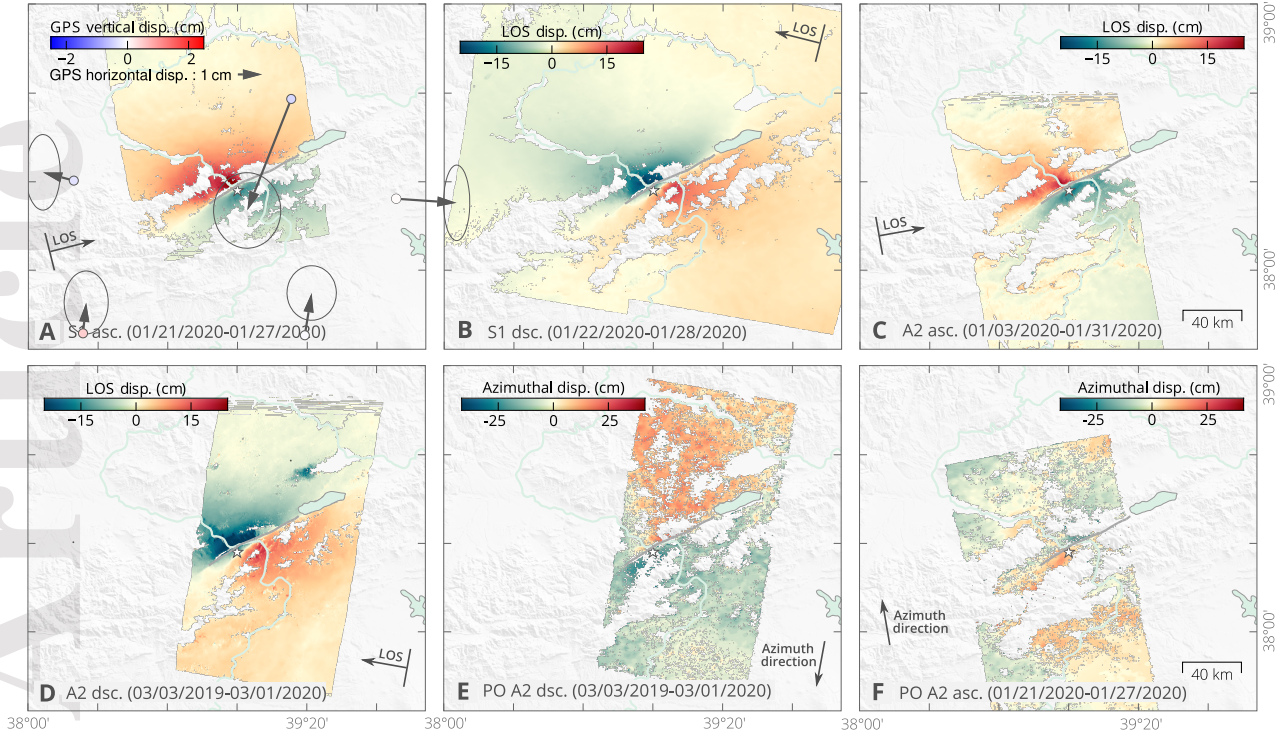


Figure 2. Observations used in this study. (a) Surface displacement in the satellite line-of-sight (LOS) direction from a Sentinel-1 (S1) ascending (asc.) interferogram, overlayed with coseismic GNSS offsets (Melgar et al., 2020). (b) Surface displacement from a Sentinel-1 descending (dsc.), (c) an ALOS-2 (A2) ascending interferogram, and (d) an ALOS-2 descending interferogram. (e) Pixel-offset (PO) surface displacement in the satellite along-track (azimuth) direction from the ALOS-2 descending pair, and (f) from the ALOS-2 ascending pair. The surface projection of the satellite LOS direction is positive in the ground-to-satellite direction.

79 inverted slip distribution. This approach allows us to describe the rupture of the Elazığ
 80 in detail, while discussing how it may have been driven by structural complexity. Finally,
 81 we also provide an updated interpretation of the seismic budget for the central EAF.

82 2 Bayesian Inference framework

83 2.1 Data

84 We derive the earthquake surface displacement from four Synthetic Aperture Radar
 85 (SAR) interferometric pairs and two SAR pixel offsets images (summarized in Table S2,
 86 Figs 2 and S1 for a closer view on the deformation). We computed two ALOS-2 ascending
 87 and descending interferograms, and two Sentinel-1 ascending and descending inter-

88 ferograms. Copernicus Sentinel-1 data have been acquired by the European Space Agency
 89 (ESA) and processed with the NSBAS software (Doin et al., 2012). ALOS-2 data are
 90 collected by the Japan Aerospace Exploration Agency (JAXA) and have been processed
 91 using the InSAR Scientific Computing Environment (ISCE) software (Rosen, 2012) aug-
 92 mented with an additional module for processing ALOS-2 data (Liang & Fielding, 2017a).

93 We also applied pixel offset tracking analysis to ALOS-2 images on both tracks (Liang
 94 & Fielding, 2017b). Resulting surface displacements have lower precision and higher noise
 95 than LOS measurements, but provide useful information on the deformation along the
 96 satellite track (azimuthal) direction. Due to snowy conditions in January, both L-band
 97 ALOS-2 and C-band Sentinel-1 data decorrelate at higher topographic elevations. Note
 98 that surface displacements derived from the InSAR data contain from 3 to 7 days of post-
 99 seismic deformation, which might affect our modeling of the coseismic phase (Ragon, Sladen,
 100 Bletery, et al., 2019; Twardzik et al., 2019). InSAR and dense pixel offsets from the ALOS-
 101 2 descending track cover 1 year of preseismic and 1 month of postseismic deformation,
 102 and thus also include long-term deformation. To improve computational efficiency, we
 103 resample InSAR observations based on model resolution (Lohman & Simons, 2005) with
 104 quadtree regions ranging from 12 km to 1.2-2 km wide. We remove data points that are
 105 within 500 m of the fault trace to prevent spatial aliasing. We estimate measurement
 106 uncertainties following Jolivet et al. (2012, Fig. S2). We also use 3 components coseis-
 107 mic GNSS offsets at 6 stations located within 120 km of the rupture (Fig. 2). These off-
 108 sets have been processed by Melgar et al. (2020) and extracted from high-rate GNSS dis-
 109 placements.

110 2.2 Fault geometry and elastic structure

111 Duman and Emre (2013) mapped the main surface trace of the Pütürge segment
 112 as a relatively continuous sinusoidal trend interrupted by small bends and step-overs whose
 113 width do not exceed the kilometer. Over the Lake Hazar releasing bend (Fig. 1c), the
 114 fault trace divides into multiple parallel lineaments that outline a 10 km wide fault zone
 115 (e.g., Garcia Moreno et al., 2011). Around Doğyanol, the fault strike abruptly changes
 116 by 10°. West of the rupture area, two major bends affect the Pütürge segment before
 117 it links to the Erkenek segment. The strike change around Doğyanol has been well out-
 118 lined by InSAR data as well (Figs 2, S1), although the rupture did not reach the sur-
 119 face. We build on these observations, as well as on the location of the aftershocks and

120 previous seismicity (Bulut et al., 2012; Melgar et al., 2020) to define the surface geom-
 121 etry of the causative fault. Hereafter, we will refer to the two bends of the causative fault
 122 as the main bend (bend of $\sim 10^\circ$ around the city of Doganyol, refer to Fig. 1c) and the
 123 second bend (east of the main bend).

124 InSAR data show largest amplitudes north of the fault (Fig. 2), suggesting that
 125 the fault is slightly dipping northward, as confirmed by the aftershocks (Melgar et al.,
 126 2020; Pousse-Beltran et al., 2020). We thus assume a fault dipping of 79° northward (Fig. 1d),
 127 from its south-western end to 30 km eastward, the dip angle linearly decreases to 75°
 128 further east. We discretize the fault into 203 triangular subfaults whose side range from
 129 1.5 km at the surface to 4-5 km at depth. We also assume a layered crustal model (Tab. S1)
 130 derived from the seismic velocity models for NE Turkey proposed by Maden (2012) and
 131 by the V_p/V_s ratio proposed by Ozer et al. (2019), and compute coseismic Green's func-
 132 tions following Zhu and Rivera (2002).

133 2.3 Bayesian Sampling of the inverse problem

134 In this study, we explore the full solution space of co-seismic slip distributions com-
 135 patible with geodetic observations in order to sample the range of plausible models. The
 136 sampling is performed with a Bayesian approach implemented in the AlTar2 package,
 137 originally formulated by Minson et al. (2013). AlTar combines the Metropolis algorithm
 138 with a tempering process to iteratively sample the solution space. A large number of sam-
 139 ples are tested in parallel at each transitional step, which is followed by a resampling step,
 140 allowing us to select only the most probable models. The probability of each sample to
 141 be selected depends on its ability to fit the observations \mathbf{d}_{obs} within the uncertainties
 142 $\mathbf{C}_\chi = \mathbf{C}_d + \mathbf{C}_p$, where \mathbf{C}_d represents the observational errors and \mathbf{C}_p the epistemic
 143 uncertainties introduced by approximations of the forward model (e.g., Minson et al.,
 144 2013; Duputel et al., 2014; Ragon et al., 2018; Ragon, Sladen, & Simons, 2019).

145 The solution space is evaluated through repeated updates of the probability den-
 146 sity function (PDF) of each sampled parameter

$$147 p(\mathbf{m}, \beta_i) \propto p(\mathbf{m}) \cdot \exp[-\beta_i \cdot \chi(\mathbf{m})], \quad (1)$$

148 where \mathbf{m} is the sampled model, $p(\mathbf{m})$ the prior information on this sample, i corresponds
 149 to each iteration and β evolves dynamically from 0 to 1 to optimize the parameter space
 exploration (Minson et al., 2013). $\chi(\mathbf{m})$ is the misfit function which quantifies the dis-

crepancies between observations and predictions within uncertainties described by the covariance matrix \mathbf{C}_χ (Tarantola, 2005; Minson et al., 2013, 2014; Duputel et al., 2014)

$$\chi(\mathbf{m}) = \frac{1}{2} [\mathbf{d}_{\text{obs}} - \mathbf{G}(\mathbf{m})]^T \cdot \mathbf{C}_\chi^{-1} \cdot [\mathbf{d}_{\text{obs}} - \mathbf{G}(\mathbf{m})]. \quad (2)$$

We solve for both slip amplitude and rake, within the assumed unrestrictive positive uniform prior distribution $p(\mathbf{m}) = \mathcal{U}(0 \text{ m}, 20 \text{ m})$ for the strike-slip parameters, and within the restrictive Gaussian prior distribution centered on zero for the dip-slip parameters $p(\mathbf{m}) = \mathcal{N}(0 \text{ m}, 1 \text{ m})$.

Ad-hoc choices of regularization, such as smoothing or moment minimization, artificially restrict the range of possible models and strongly bias the inferred slip distributions towards simplistic overly-smoothed solutions (e.g., Du et al., 1992; Causse et al., 2010). In our approach, we do not impose any type of prior regularization and explore the entire solution space, i.e. the entire range of possible slip models. The final output thus consists in a series of models sampled from among the most plausible models of the full solution space. To explore the results, we consider probabilistic variables, such as a combination of the mean of the sampled models and the associated posterior uncertainty (standard deviation).

2.4 Accounting for epistemic uncertainties

Our estimates of fault slip are driven by the quality and quantity of observations, but also by the way we build the forward model and any other prior information we include in the problem. Any prior choice made to evaluate the Green's function (including problem parameterization and description of the Earth interior) will have a significant impact on inferred model parameters (e.g., Beresnev, 2003; Hartzell et al., 2007; Yagi & Fukahata, 2008; Razafindrakoto & Mai, 2014; Duputel et al., 2014; Gallović et al., 2015; Diao et al., 2016; Mai et al., 2016). So-called epistemic uncertainties stem from our imperfect description, or simplification, of the parameters describing the Earth interior, such as crustal properties (e.g., rheology), fault geometry or regional characteristics (e.g., topography, Langer et al., 2020). In contrast, aleatoric uncertainties will derive from random, or unknown, processes. In this study, we account for the epistemic uncertainties caused by our poor knowledge of the fault dip, the fault position, and the elastic layered crustal structure, following the methodologies presented by Duputel et

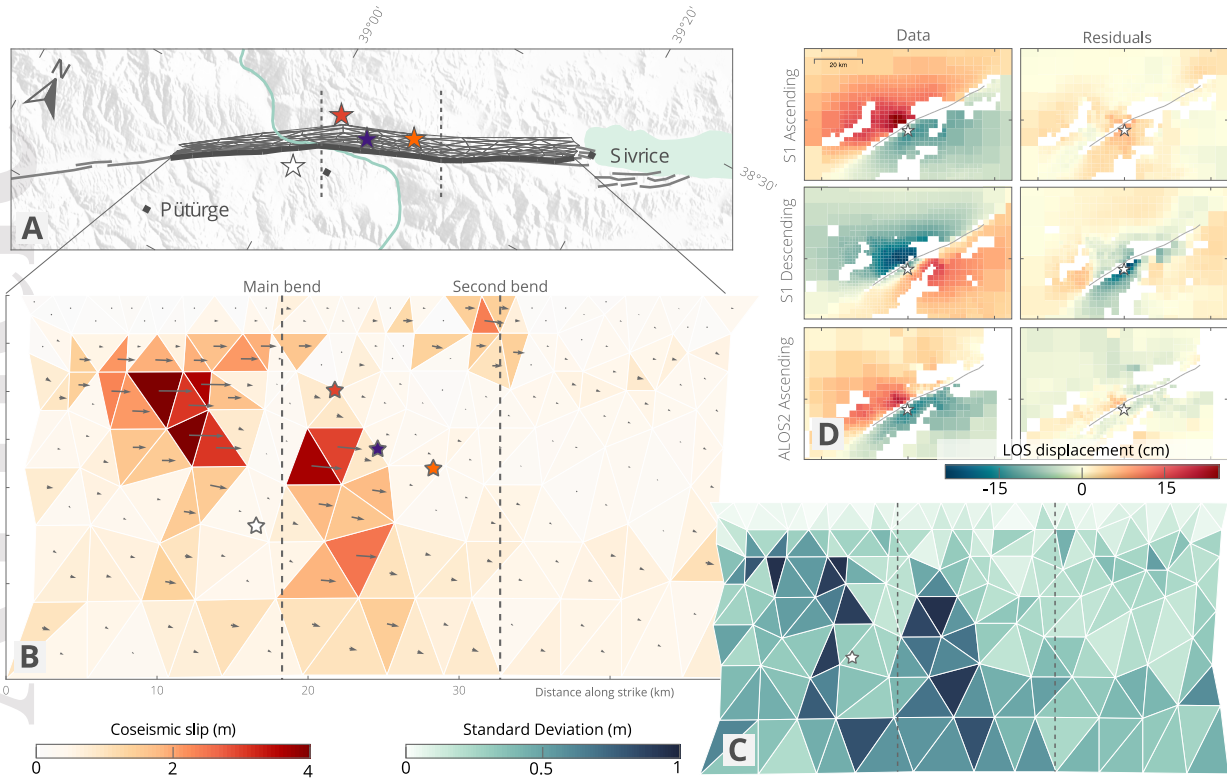


Figure 3. Inferred average slip model and associated posterior uncertainty for the Elazığ earthquake. (a) Map view of the fault trace, subfaults contours at depth and local setting. Possible epicenters are shown with white, red, purple and orange stars (from left to right on the map), respectively from GCMT, Jamalreyhani et al. (2020), KOERI and AFAD (2020). (b) Depth view of the average total slip amplitudes and directions. (c) Standard deviation of the inferred strike-slip parameters. (d) Observed and predicted surface displacement in the LOS direction from Sentinel-1 ascending and descending, and ALOS-2 ascending, InSAR.

al. (2014); Ragon et al. (2018); Ragon, Sladen, and Simons (2019). A part of the aleatoric uncertainties is also quantified with our stochastic approach.

We assume 1 km uncertainty (1σ) in the location of the surface projection of the fault, and 5° uncertainty (1σ) in the fault dip, the fault rotating as a whole around its assumed dip (Fig. 1). We assume uncertainties on the shear modulus for every layer (Poisson's ratio is held constant within each layer), the uncertainty decreasing with depth (Fig. 1, Tab. S1).

186 **3 Results**

187 We infer primarily strike-slip fault slip (Fig. 3). Most of the slip is imaged around
 188 the main bend (localized around the city of Doganyol, Fig. 3a). Slip exceeds 3 m within
 189 two slip patches, from 2 to 10 km depth west of the main bend and from 7 to 10 km depth
 190 east of the main bend. Associated posterior uncertainty for these patches can reach up
 191 to ~ 1 m for highest amplitudes (Fig. 3c). West of the main bend, the rupture extends
 192 down to greater depths (7 - 15 km) with moderate slip amplitudes of ~ 2 m. At depth,
 193 the posterior model uncertainty reaches up to 1 m. The posterior marginal distributions
 194 all show well-delineated Gaussian shapes (Fig. S3), even for the smallest slip amplitudes.
 195 The posterior PDFs on subfaults in between these two main slip patches indicate well
 196 resolved very low slip amplitudes (Fig. S3), suggesting that the two patches are discon-
 197 nected (Fig. 3c).

198 One other narrow slip patch can be observed west of the main bend, at the loca-
 199 tion of the second bend. Slip is imaged from the surface to 4-km-depth, with maximum
 200 amplitudes reaching 2.5 m at the surface, and with relatively small posterior uncertainty.
 201 This patch is not connected with the main slip patches, and does not seem to correspond
 202 to any $M_w > 4$ aftershock (relocated by Melgar et al., 2020; Pousse-Beltran et al., 2020).
 203 This slip may be coseismic or afterslip (given that the InSAR data span a period up to
 204 one month after the mainshock).

205 Observations are well fit by the predictions of our model (Table S3, Figs. 3(d), S5,
 206 S6, S7 and S8 for the InSAR and GNSS data respectively), within the assumed uncer-
 207 tainties and possible remaining noise (in particular for the pixel-offset data). Account-
 208 ing for epistemic uncertainties mitigates overfitting (Ragon et al., 2018). Residuals are
 209 expected to be larger than if epistemic biases are neglected. The descending interfero-
 210 grams present larger residuals (Figs. S5, S6, S7) because the assumed fault geometry is
 211 primarily constrained by ascending data, and the descending imaging geometry is less
 212 favorably oriented (the LOS has a 45° angle with the fault strike).

213 We also infer the slip distribution of the Elazığ earthquake assuming a planar fault
 214 structure dipping of 85° towards the north and embedded within a homogeneous half
 215 space, without introducing any epistemic uncertainty (Fig S9). Unlike our preferred model,
 216 the slip is concentrated in a single shallow and extended slip patch with low posterior
 217 uncertainty. Highest amplitudes (up to 3.5 m) are reached above the main bend, from

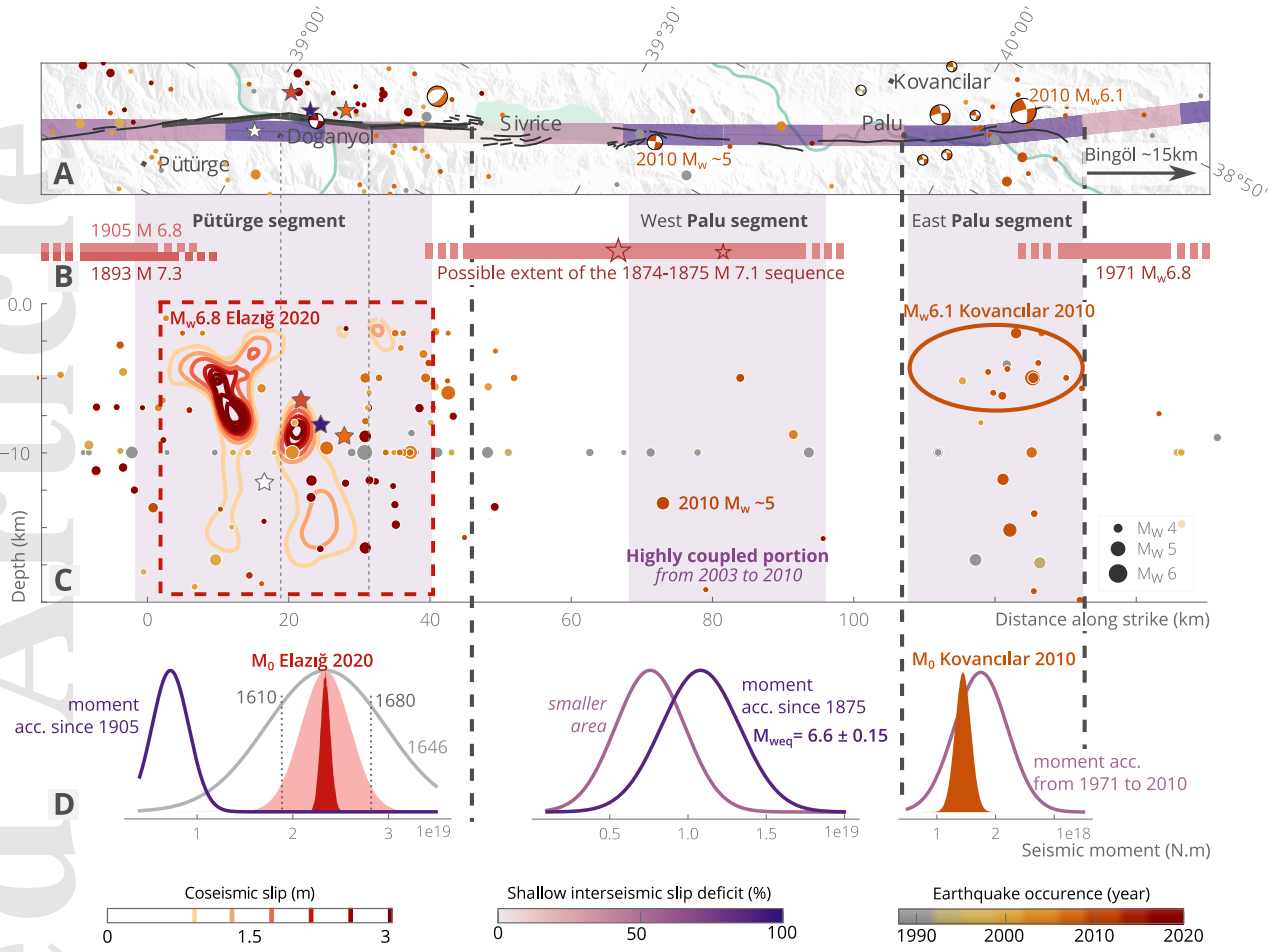


Figure 4. Comparison between the spatial distributions of the 2020 Elazığ earthquake rupture, historical earthquakes, highly coupled sections of the EAF, and seismic moment accumulated since last historical rupture in relation with seismic moment released by the most recent event. (continued)

1.5 to 9 km depth. Low slip values are inferred at depths greater than 10 km and lower than 1.5 km. Some slip is also inferred around the second bend. As expected, the fit of the predicted displacement to the observations is good (Table S3, Figs. S10, S11, S12 and S13), descending interferograms still presenting larger residuals, and slightly better than with our preferred inference.

4 Discussion and Conclusion

Figure 4. Comparison between the spatial distributions of the 2020 Elazığ earthquake rupture, historical earthquakes, highly coupled sections of the EAF, and seismic moment accumulated since last historical rupture in relation with seismic moment released by the most recent event. (A) Map view of two segments the East Anatolian Fault (black lines), overlayed with historical and recent seismicity from 1900 to January 2020 (Retrieved from AFAD, 2020; NEIC, 2020; Melgar et al., 2020), shallow interseismic slip deficit (Bletery et al., 2020) and our assumed fault trace for the 2020 Elazığ event (thick black line). (B) Possible rupture extents for the 4 most recent $M_w > 6.5$ earthquakes that struck the mapped segments of the EAF before the Elazığ event, inferred from Ambraseys (1989); Hubert-Ferrari et al. (2020). Red stars denote the locations of the mainshock and aftershock of the 1874 sequence (Ambraseys, 1989). Fault segments of the central EAF are indicated, from Duman and Emre (2013). (C) Depth extent of the slip amplitude inferred for the 2020 Elazığ event (Fig. 3), along with the highly coupled sections of the EAF between 2003 and 2010 (Bletery et al., 2020), and the possible extent of the 2010 $M_w 6.1$ Kovancılar earthquake estimated from the spatial coverage of aftershocks and basic scaling laws (Wells & Coppersmith, 1994; Tan et al., 2011), as well as historical and recent seismicity from 1900 to January 2020. (D) For highly coupled portion of each segment, comparison of PDFs of accumulated seismic moment since last historical rupture (in purple), with the seismic moment (M_0) of last recent earthquakes, i.e. the 2020 Elazığ (red) or 2010 Kovancılar (orange) events. For the Pütürge segment, the PDF and mean of accumulated seismic moment since the time needed to accumulate the Elazığ event M_0 are shown in gray, and the PDFs of the Elazığ M_0 are derived from our preferred slip model (red), with a version accounting for uncertainties in the shear modulus ($\mu = 2.8 \pm 0.3 \cdot 10^1$ GPa, light red).

224 4.1 A stochastic view of the 2020 Elazığ coseismic rupture

225 Assuming a realistic fault geometry and cristal structure, and accounting for re-
 226 lated epistemic uncertainties, we estimate the slip distribution of the 2020 Elazığ earth-
 227 quake with a Bayesian inference approach. We show that the coseismic rupture affects
 228 almost the full width of the Pütürge segment, down to 15-km-depth, with a geodetic mo-
 229 ment $M_0 = 2.34 \pm 0.25 \cdot 10^{19}$ N · m and an equivalent moment magnitude of 6.84 ($\mu =$
 230 $2.8 \pm 0.3 \cdot 10^1$ GPa). Two disconnected slip patches host most of the slip: one patch shows
 231 slip exceeding 3 m from ~ 3 to ~ 10 km depth east of the main bend, while the second
 232 slip patch extends from 7-km-depth down to 15-km-depth with slip amplitudes larger
 233 than 2 m just west of the main bend (Fig. 3).

234 A large shallow slip (0–5 km, 2.5 m in amplitude) is also imaged around the sec-
 235 ond bend. While the standard deviation associated with this shallow slip patch is rel-
 236 atively small, its amplitude is poorly constrained by scarce, and possibly noisy, data points
 237 largely affected by snowy conditions (Figs. S5, S6, S7). Some of our InSAR data cov-
 238 ering up to one month after the mainshock, some imaged deformation, such as this shal-
 239 low patch, might actually be postseismic. Yet, the surface displacement from 1 week to
 240 5 months after the mainshock does not reach more than a few centimeters (Fig. S14),
 241 suggesting that, if afterslip occurred, it was in the hours following the mainshock and
 242 with a limited amplitude (as the amplitude of early afterslip often scales with the longer
 243 term postseismic deformation, e.g., Twardzik et al., 2019), thus probably not excessively
 244 affecting our slip estimates.

245 The inferred slip distribution changes significantly if we assume a planar fault em-
 246 bedded in a homogeneous crust and we neglect uncertainties stemming from the assump-
 247 tion of a simplified Earth interior. In particular, a single and shallower slip patch is in-
 248 ferred around the epicenter, no slip larger than 50 cm being imaged above 2 km, or larger
 249 than 80 cm below 10 km depth. The pronounced slip deficit imaged when assuming a
 250 simplified forward model (Fig. S15) might suggest that the shallow slip deficit observed
 251 by Pousse-Beltran et al. (2020) may be an artifact deriving from modeling choices, as
 252 proposed by Xu et al. (2016) and Ragon et al. (2018).

253 The location of the epicenter, as estimated from different institutions and authors,
 254 comes with more than 16 and 20 kilometers uncertainty in depth and position, respec-
 255 tively (e.g., Jamalreyhani et al., 2020; Tatar et al., 2020). While some models proposed
 256 a location around the main bend, many others proposed epicenters rather located in be-
 257 tween the two bends (Fig. 3). Robust interpretation on rupture directivity is largely af-
 258 fected by uncertainty in epicenters location, although our results suggest the rupture of
 259 the Elazığ earthquake might be mostly unilateral to the SW.

260 Our estimates of the pattern of fault slip differ from other estimates based on sim-
 261 ilar data (e.g., Melgar et al., 2020; Pousse-Beltran et al., 2020; Cheloni & Akinci, 2020;
 262 Doğru et al., 2020). Our preferred model is very different from Pousse-Beltran et al. (2020);
 263 Cheloni and Akinci (2020); Doğru et al. (2020), where peak slip reaches only 2 m over
 264 the main bend. In contrast, our preferred model shares many characteristics with the
 265 preferred one of Melgar et al. (2020), especially for the peak slip location and the over-

all shape of the ruptured areas, although they image large slip values east of the KO-
 ERI epicenter. Melgar et al. (2020) preferred model being primarily driven by high-rate
 GNSS data and assuming a 1D crustal structure, these shared characteristics suggest that
 assuming a layered crustal model is necessary to infer robust slip estimates in this re-
 gion.

4.2 Structurally driven slip on the Pütürge segment

Fault segmentation and bends are thought to act as geometric barriers that can
 influence, or even drive, rupture initiation, termination and propagation (e.g., G. King
 & Nabelek, 1985; A. A. Barka & Kadinsky-Cade, 1988; Wesnousky, 2006; Duan & Oglesby,
 2005; Aochi et al., 2002; Perrin et al., 2016; Klinger, 2010). Similarly, creeping sections
 might act as barriers to earthquake propagation (e.g., G. C. P. King, 1986; Chlieh et al.,
 2008; Perfettini et al., 2010; Kaneko et al., 2010).

The coseismic rupture of the Elazığ earthquake likely started in a relatively planar portion of the fault, in between its two main bends (refer to Fig. 3, Jamalreyhani et al., 2020). Similarly, peak slip amplitudes and most of the slip are located in relatively smooth areas, and surround the main bend where well-resolved low slip values have been imaged. The absence of slip in the main bend is a robust characteristic of our preferred slip model, which has not been imaged in previous studies (e.g., Melgar et al., 2020). The event thus likely ruptured a first portion of the Pütürge segment, stopped at the main bend acting as a barrier, and then broke a second portion, a process that has been observed in numerical simulations (e.g., Kato et al., 1999; Duan & Oglesby, 2005). A perturbation of the rupture propagation by the main bend well correlates with the apparent rupture velocity decrease around the geometrical complexity (imaged by back-projection of waveforms, Pousse-Beltran et al., 2020), and the two distinct peaks of the source time function (automatically determined, Vallée & Douet, 2016).

Slip slowly decreases towards Lake Hazar (Fig. 4). Aftershocks activity also declines abruptly at the basin boundary (Melgar et al., 2020; Jamalreyhani et al., 2020). The pull-apart basin hosting Lake Hazar might thus have acted as a geometrical barrier to the ruptured asperity (as also observed for the Haiyuan fault, China, Liu-Zeng et al., 2007; Jolivet et al., 2013). To the west, no specific geometrical complexity is imaged at the sur-

296 face, and the rupture may have stopped at the maximum length of the fault segment (Klinger,
 297 2010).

298 Finally, the location of the main bend also corresponds to the portion of the EAF
 299 that shows maximum shallow interseismic slip deficit ($>90\%$, Fig. 4). Inferred slip partly
 300 overlays this portion of maximum slip deficit, but the coseismic rupture also extends over
 301 moderately coupled regions (30-40%) at greater depths (from 8 to 15-km-depth). The
 302 second bend, to the northeast of the main bend (Fig. 3), is also surrounded by large (>2
 303 m) slip amplitudes at shallow depths.

304 Altogether, these observations suggest that the distribution of subsurface fault slip
 305 during the Elazığ earthquake may largely reflect complexities in the fault geometry. Rup-
 306 tured portions appear to be relatively smooth. In contrast, the main fault bend likely
 307 acted as a barrier to rupture propagation, over which no slip has been imaged, similarly
 308 to the structure responsible for the pull-apart basin of Lake Hazar. The bend is not prone
 309 either to aseismic slip (at least at shallow depths). The deepest imaged slip patch, down
 310 to 15-km-depth, confirms that the seismogenic depth is deeper than 10 km for the cen-
 311 tral EAF (Bulut et al., 2012). Our results do not seem to corroborate the shallow lock-
 312 ing depth (full creep below 5 km) inferred by Cavalié and Jónsson (2014). This behav-
 313 ior appears similar to the NAF, where large earthquakes occur on faults also prone to
 314 aseismic slip (Cakir et al., 2005, 2014b; Schmittbuhl et al., 2016).

315 4.3 Seismic potential of the Palu segment

316 From Pütürge to Bingöl, interseismic slip deficit above 5-km-depth varies along strike,
 317 as inferred from geodetic data from 2003 to 2010 (Bletery et al., 2020, Figs 4, S16). Three
 318 main sections of large shallow interseismic slip deficit ($>70\%$) are clearly distinct: one
 319 on the Pütürge segment, another on the West Palu segment, and a last one east of the
 320 city of Palu, on the East Palu segment. Before the Elazığ event, this portion of the EAF
 321 was struck by 4 large earthquakes in the last 200 years. Two $M \sim 6.8$ and $M \sim 7.3$ oc-
 322 curred west of Lake Hazar in 1893 and 1905 (Ambraseys, 1989). In 1874-1875, a sequence
 323 of two $M \sim 7.1$ and $M \sim 6.7$ likely struck the region between Sivrice and Palu (Ambraseys,
 324 1989; Cetin et al., 2003; Hubert-Ferrari et al., 2017). East of the locality of Palu, the re-
 325 gion around the city of Bingöl was affected by a $M_w 6.8$ in 1971 (Ambraseys, 1989; Am-
 326 braseys & Jackson, 1998).

Slip deficit has accumulated on the EAF since these recent historical ruptures, and the newly coupled portions (from 2003 to 2010) are preferably located in between the historically ruptured segments (Bletery et al., 2020). The 2010 M_w 6.1 earthquake that occurred near Kovancilar (Akkar et al., 2011) appears to have filled the possible seismic gap between the 1874 sequence and the 1971 Bingöl event (Fig. 4B). Similarly, the extent of the Elazığ rupture well overlays with a highly coupled portion of the EAF, and it may have filled a possible gap between the 1893/1905 earthquakes and the 1874 sequence (Melgar et al., 2020; Duman & Emre, 2013).

We compare the seismic moment accumulated since the possible last historic rupture of the Pütürge segment (1905) with the seismic moment released during the 2020 Elazığ earthquake (Fig. 4D). To do so, we calculate the seismic moment for the area ruptured by the event according to our slip model, and account for uncertainties in ruptured area ($\sigma = 3 \text{ km}^2$), shear modulus ($\mu = 2.8 \pm 0.3 \cdot 10^1 \text{ GPa}$), coupling and slip rates (according to Bletery et al., 2020). The moment released by the 2020 event is largely greater than the one accumulated since 1905 ($2.34 \pm 0.25 >> 0.72 \pm 0.19 \cdot 10^{19} \text{ N} \cdot \text{m}$). Around 475 years (since 1646) would be necessary to accumulate the moment released by the Elazığ earthquake, assuming constant coupling and slip rates, confirming that the Pütürge segment did probably not rupture during the last historical events, and effectively was a seismic gap. We make the same comparison for the East Palu segment, and show that the moment released by the 2010 M_w 6.1 Kovancilar earthquake well matches the moment accumulated from the 1971 Bingöl event to 2010 ($1.58 \pm 0.2 \approx 2.19 \pm 0.56 \cdot 10^{18} \text{ N} \cdot \text{m}$, Fig. 4D), suggesting this portion of the EAF actually ruptured during the 1971 event, and that all of the accumulated moment has been released at the time of the Kovancilar earthquake. Since 2010, the seismic moment of the East Palu segment likely accumulated again to reach $4.48 \pm 0.5 \cdot 10^{17} \text{ N} \cdot \text{m}$, which corresponds to a $M_w \approx 5.73$.

Although the portions of the EAF that have been affected by the Elazığ and Kovancilar events show seismic activity in the 20 years preceding these events, the West Palu segment is characterized by relatively low seismic activity (Fig. 4). Together with the low slip deficit at depth (or shallow 5 km locking depth, Cavalié & Jónsson, 2014; Bletery et al., 2020), the lack of seismicity might suggest that the West Palu segment is creeping. However, this segment also shows large interseismic slip deficit in its shallow portion (< 5-km-depth), and at greater depths even larger than for the Pütürge segment (before the 2020 event, Bletery et al., 2020, Fig. S16). Ground shaking maps de-

rived from press reports and testimonies suggest the 1874 sequence likely initiated at depth just west of Lake Hazar (Ambraseys, 1989), near the epicenter of a $M_w \sim 5$ earthquake that occurred in 2010. The West Palu segment is thus capable of producing large earthquakes. Cheloni and Akinci (2020) also suggest that the Elazığ event led to an increase in the Coulomb stress of the Palu segment. Altogether, these observations suggest that the West Palu segment of the central EAF is likely seismogenic. If it were to rupture, the moment accumulated since 1875 on the highly coupled portion is of $7.58 \pm 2.2 \cdot 10^{18} \text{ N} \cdot \text{m}$ (light purple in Fig. 4D), and may reach $1.08 \pm 0.25 \cdot 10^{19} \text{ N} \cdot \text{m}$ if the rupture extends from Lake Hazar to the city of Palu (dark purple in Fig. 4D), which would correspond to a $M_w \sim 6.6 \pm 0.15$ earthquake.

Acknowledgments

The slip model and data are available at <https://doi.org/10.5281/zenodo.4114109>. We thank an anonymous reviewer and Brendan Crowell for thorough reviews. We are very grateful to Diego Melgar and Brendan Crowell who calculated and provided the GNSS offsets for the coseismic deformation, and their relocated aftershocks catalog, which are both available in Melgar et al. (2020). GNSS data were made available from the Turkish National Permanent GNSS/RTK Network (TUSAGA-Aktif/CORS-TR administrated by General Directorate of Land Registry and Cadastre-TKGM and General Directorate of Mapping-HGM, Ankara, Turkey), thanks to Prof. Tuncay Taymaz and Prof. Taylan calan. Initial aftershocks and phase-arrival catalog has been provided by the Disaster and Emergency Management Presidency of Turkey (AFAD, 2020) for the period 24 January 2020 11 February 2020, and historical/background seismicity catalog was provided by BU-KOERI (<http://www.koeri.boun.edu.tr/sismo/2/en/>) for Turkey from 1992 to 2020. This work contains modified Copernicus data from the Sentinel-1A and -1B satellites provided by the European Space Agency (ESA) that are accessible at `earth.esa.int/eogateway/`. Original ALOS-2 data and products are copyright JAXA and provided under JAXA ALOS Research Announcement 6 (RA6) project 3278. The Bayesian simulations were performed with the Altar2 package (github.com/ljun99/altar2-documentation, only accessible via github at publication date). The Classic Slip Inversion (CSI, github.com/jolivetr/csi, only accessible via github at publication date) Python library (Jolivet et al., 2014) was used to build inputs for the Bayesian algorithm, in particular to compute Green's functions. The python module PyDistMesh has been used to build the fault

geometry (Persson & Strang, 2004). Figures were generated with the Matplotlib and Seaborn ([doi:10.5281/zenodo.1313201](https://doi.org/10.5281/zenodo.1313201)) Python libraries and with the Generic Mapping Tools library (Wessel et al., 2019). MS was partially supported by the National Aeronautics and Space Administration under Grant No. 80NSSC19K1499. EF was partially supported by the National Aeronautics and Space Administration Earth Surface and Interior focus area under Grant No. 80NM0018D0004. QB work has been supported by the French government, through the UCA JEDI Investments in the Future project managed by the National Research Agency (ANR) ANR-15-IDEX-01, the ANR S5 Grant No. ANR-19-CE31-0003, and the ANR JCJC E-POST Grant No. ANR-14-CE03-002-01JCJC.

References

- AFAD. (2020). *AFAD Earthquake catalogue (1900–Feb 2020)*, Prime Ministry, Disaster and Emergency Management Pres-. <https://deprem.afad.gov.tr/depremkatalogu?lang=en#>.
- Akkar, S., Aldemir, A., Askan, A., Bakır, S., Canbay, E., Demirel, İ. O., ... Yenier, E. (2011). 8 March 2010 Elazığ-Kovancılar (Turkey) Earthquake: Observations on Ground Motions and Building Damage. *Seismological Research Letters*, 82(1), 42–58. doi: 10.1785/gssrl.82.1.42
- Aktug, B., Ozener, H., Dogru, A., Sabuncu, A., Turgut, B., Halicioglu, K., ... Hava- zli, E. (2016). Slip rates and seismic potential on the East Anatolian Fault System using an improved GPS velocity field. *Journal of Geodynamics*, 94-95, 1–12. doi: 10.1016/j.jog.2016.01.001
- Ambraseys, N. N. (1970). Some characteristic features of the Anatolian fault zone. *Tectonophysics*, 9(2), 143–165. doi: 10.1016/0040-1951(70)90014-4
- Ambraseys, N. N. (1989). Temporary seismic quiescence: SE Turkey. *Geophysical Journal International*, 96(2), 311–331. doi: 10.1111/j.1365-246X.1989.tb04453.x
- Ambraseys, N. N., & Jackson, J. A. (1998). Faulting associated with historical and recent earthquakes in the Eastern Mediterranean region. *Geophysical Journal International*, 133(2), 390–406. doi: 10.1046/j.1365-246X.1998.00508.x
- Aochi, H., Madariaga, R., & Fukuyama, E. (2002). Effect of normal stress during rupture propagation along nonplanar faults. *Journal of Geophysical Research: Solid Earth*, 107(B2), ESE 5-1-ESE 5-10. doi: 10.1029/2001JB000500

- 424 Armijo, R., Meyer, B., Hubert, A., & Barka, A. (1999). Westward propagation
 425 of the North Anatolian fault into the northern Aegean: Timing and kine-
 426 matics. *Geology*, 27(3), 267–270. doi: 10.1130/0091-7613(1999)027<0267:
 427 WPOTNA>2.3.CO;2
- 428 Barka, A. (1996). Slip distribution along the North Anatolian fault associated with
 429 the large earthquakes of the period 1939 to 1967. *Bulletin of the Seismological
 430 Society of America*, 86(5), 1238–1254.
- 431 Barka, A. A., & Kadinsky-Cade, K. (1988). Strike-slip fault geometry in Turkey and
 432 its influence on earthquake activity. *Tectonics*, 7(3), 663–684. doi: 10.1029/
 433 TC007i003p00663
- 434 Basilic, R., Kastelic, V., Demircioglu, M. B., Garcia Moreno, D., Nemser, E. S.,
 435 Petricca, P., ... Wössner, J. (2013). The European Database of Seismogenic
 436 Faults (EDSF) compiled in the framework of the Project SHARE.
 437 doi: 10.6092/INGV.IT-SHARE-EDSF
- 438 Beresnev, I. A. (2003). Uncertainties in Finite-Fault Slip Inversions: To What Ex-
 439 tent to Believe? (A Critical Review). *Bulletin of the Seismological Society of
 440 America*, 93(6), 2445–2458. doi: 10.1785/0120020225
- 441 Bletery, Q., Cavalié, O., Nocquet, J.-M., & Ragon, T. (2020). Distribution of In-
 442 terseismic Coupling Along the North and East Anatolian Faults Inferred From
 443 InSAR and GPS Data. *Geophysical Research Letters*, 47(16), e2020GL087775.
 444 doi: 10.1029/2020GL087775
- 445 Bulut, F., Bohnhoff, M., Eken, T., Janssen, C., Kılıç, T., & Dresen, G. (2012).
 446 The East Anatolian Fault Zone: Seismotectonic setting and spatiotemporal
 447 characteristics of seismicity based on precise earthquake locations. *Journal of
 448 Geophysical Research: Solid Earth*, 117(B7). doi: 10.1029/2011JB008966
- 449 Cakir, Z., Akoglu, A. M., Belabbes, S., Ergintav, S., & Meghraoui, M. (2005).
 450 Creeping along the Ismetpasa section of the North Anatolian fault (Western
 451 Turkey): Rate and extent from InSAR. *Earth and Planetary Science Letters*,
 452 238(1), 225–234. doi: 10.1016/j.epsl.2005.06.044
- 453 Cakir, Z., Ergintav, S., Akoglu, A. M., Çakmak, R., Tatar, O., & Meghraoui, M.
 454 (2014a). InSAR velocity field across the North Anatolian Fault (eastern
 455 Turkey): Implications for the loading and release of interseismic strain accumu-
 456 lation. *Journal of Geophysical Research: Solid Earth*, 119(10), 7934–7943. doi:

457 10.1002/2014JB011360

- 458 Cakir, Z., Ergintav, S., Akoğlu, A. M., Çakmak, R., Tatar, O., & Meghraoui, M.
 459 (2014b). InSAR velocity field across the North Anatolian Fault (eastern
 460 Turkey): Implications for the loading and release of interseismic strain accumu-
 461 lation. *Journal of Geophysical Research: Solid Earth*, 119(10), 7934–7943. doi:
 462 10.1002/2014JB011360
- 463 Causse, M., Cotton, F., & Mai, P. M. (2010). Constraining the roughness degree of
 464 slip heterogeneity. *Journal of Geophysical Research: Solid Earth*, 115(B5). doi:
 465 10.1029/2009JB006747
- 466 Cavalié, O., & Jónsson, S. (2014). Block-like plate movements in eastern Anato-
 467 lia observed by InSAR. *Geophysical Research Letters*, 26–31. doi: 10.1002/
 468 2013GL058170@10.1002/(ISSN)1944-8007.GRLeditorhghlts2014
- 469 Cetin, H., Güneyli, H., & Mayer, L. (2003). Paleoseismology of the Palu–Lake Hazar
 470 segment of the East Anatolian Fault Zone, Turkey. *Tectonophysics*, 374(3),
 471 163–197. doi: 10.1016/j.tecto.2003.08.003
- 472 Cheloni, D., & Akinci, A. (2020). Source modelling and strong ground motion simu-
 473 lations for the January 24, 2020, Mw 6.8 Elazığ earthquake, Turkey. *Geophys-
 474 ical Journal International*. doi: 10.1093/gji/ggaa350
- 475 Chlieh, M., Avouac, J. P., Sieh, K., Natawidjaja, D. H., & Galetzka, J. (2008). Het-
 476 erogeneous coupling of the Sumatran megathrust constrained by geodetic and
 477 paleogeodetic measurements. *Journal of Geophysical Research: Solid Earth*,
 478 113(B5). doi: 10.1029/2007JB004981
- 479 Diao, F., Wang, R., Aochi, H., Walter, T. R., Zhang, Y., Zheng, Y., & Xiong, X.
 480 (2016). Rapid kinematic finite-fault inversion for an Mw 7+ scenario earth-
 481 quake in the Marmara Sea: An uncertainty study. *Geophysical Journal Inter-
 482 national*, 204(2), 813–824. doi: 10.1093/gji/ggv459
- 483 Doğru, A., Bulut, F., Yalıtrak, C., & Aktuğ, B. (2020). Slip distribution of
 484 the 2020 Elazığ Earthquake (MW 6.75) and its influence on earthquake
 485 hazard in the Eastern Anatolia. *Geophysical Journal International*. doi:
 486 10.1093/gji/ggaa471
- 487 Doin, M.-P., Lodge, F., Guillaso, S., Jolivet, R., Lasserre, C., Ducret, G., ... Pinel,
 488 V. (2012). Presentation Of The Small Baseline NSBAS Processing Chain On A
 489 Case Example: The ETNA Deformation Monitoring From 2003 to 2010 Using

- 490 ENVISAT Data. , 697, 98.
- 491 Du, Y., Aydin, A., & Segall, P. (1992). Comparison of various inversion techniques
492 as applied to the determination of a geophysical deformation model for the
493 1983 Borah Peak earthquake. *Bulletin of the Seismological Society of America*,
494 82(4), 1840–1866.
- 495 Duan, B., & Oglesby, D. D. (2005). Multicycle dynamics of nonplanar strike-slip
496 faults. *Journal of Geophysical Research: Solid Earth*, 110(B3). doi: 10.1029/
497 2004JB003298
- 498 Duman, T. Y., & Emre, Ö. (2013). The East Anatolian Fault: Geometry, segmen-
499 tation and jog characteristics. *Geological Society, London, Special Publications*,
500 372(1), 495–529. doi: 10.1144/SP372.14
- 501 Duputel, Z., Agram, P. S., Simons, M., Minson, S. E., & Beck, J. L. (2014). Ac-
502 counting for prediction uncertainty when inferring subsurface fault slip. *Geo-*
503 *physical Journal International*, 197(1), 464–482. doi: 10.1093/gji/ggt517
- 504 Dziewonski, A. M., Chou, T.-A., & Woodhouse, J. H. (1981). Determination of
505 earthquake source parameters from waveform data for studies of global and
506 regional seismicity. *Journal of Geophysical Research: Solid Earth*, 86(B4),
507 2825–2852. doi: 10.1029/JB086iB04p02825
- 508 Gallovič, F., Imperatori, W., & Mai, P. M. (2015). Effects of three-dimensional
509 crustal structure and smoothing constraint on earthquake slip inversions: Case
510 study of the Mw6.3 2009 L'Aquila earthquake. *Journal of Geophysical Re-*
511 *search: Solid Earth*, 120(1), 2014JB011650. doi: 10.1002/2014JB011650
- 512 Garcia Moreno, D., Hubert, A., Moernaut, J., Fraser, J., Boes, X., Van Daele,
513 M., ... De Batist, M. (2011). Structure and evolution of Lake Hazar pull-
514 apart Basin along the East Anatolian Fault. *Basin Research*, 23. doi:
515 10.1111/j.1365-2117.2010.00476.x
- 516 Hartzell, S., Liu, P., Mendoza, C., Ji, C., & Larson, K. M. (2007). Stability and
517 Uncertainty of Finite-Fault Slip Inversions: Application to the 2004 Parkfield,
518 California, Earthquake. *Bulletin of the Seismological Society of America*,
519 97(6), 1911–1934. doi: 10.1785/0120070080
- 520 Hubert-Ferrari, A., Lamair, L., Hage, S., Schmidt, S., Çağatay, M. N., & Avşar, U.
521 (2020). A 3800 yr paleoseismic record (Lake Hazar sediments, eastern Turkey):
522 Implications for the East Anatolian Fault seismic cycle. *Earth and Planetary*

- 523 *Science Letters*, 538, 116152. doi: 10.1016/j.epsl.2020.116152
- 524 Hubert-Ferrari, A., El-Ouahabi, M., Garcia-Moreno, D., Avşar, U., Altınok, S.,
 525 Schmidt, S., ... Çağatay, M. N. (2017). Earthquake imprints on a lacustrine
 526 deltaic system: The Kürk Delta along the East Anatolian Fault (Turkey).
 527 *Sedimentology*, 64(5), 1322–1353. doi: 10.1111/sed.12355
- 528 Hussain, E., Wright, T. J., Walters, R. J., Bekaert, D. P. S., Lloyd, R., & Hooper,
 529 A. (2018). Constant strain accumulation rate between major earthquakes
 530 on the North Anatolian Fault. *Nature Communications*, 9(1), 1392. doi:
 531 10.1038/s41467-018-03739-2
- 532 Jamalreyhani, M., Büyükkapınar, P., Cesca, S., Dahm, T., Sudhaus, H., Rezapour,
 533 M., ... Heimann, S. (2020). Seismicity related to the eastern sector of Ana-
 534 tolian escape tectonic: The example of the 24 January 2020 Mw 6.77 Elazığ-
 535 Sivrice earthquake. *Solid Earth Discussions*, 1–22. doi: 10.5194/se-2020-55
- 536 Jolivet, R., Duputel, Z., Riel, B., Simons, M., Rivera, L., Minson, S. E., ... Fielding,
 537 E. J. (2014). The 2013 Mw 7.7 Balochistan Earthquake: Seismic Potential
 538 of an Accretionary Wedge. *Bulletin of the Seismological Society of America*,
 539 104(2), 1020–1030. doi: 10.1785/0120130313
- 540 Jolivet, R., Lasserre, C., Doin, M.-P., Guillaso, S., Peltzer, G., Dailu, R., ... Xu,
 541 X. (2012). Shallow creep on the Haiyuan Fault (Gansu, China) revealed by
 542 SAR Interferometry. *Journal of Geophysical Research: Solid Earth*, 117(B6),
 543 B06401. doi: 10.1029/2011JB008732
- 544 Jolivet, R., Lasserre, C., Doin, M. P., Peltzer, G., Avouac, J. P., Sun, J., & Dailu,
 545 R. (2013). Spatio-temporal evolution of aseismic slip along the Haiyuan fault,
 546 China: Implications for fault frictional properties. *Earth and Planetary Science
 547 Letters*, 377–378, 23–33. doi: 10.1016/j.epsl.2013.07.020
- 548 Kaneko, Y., Avouac, J.-P., & Lapusta, N. (2010). Towards inferring earthquake pat-
 549 terns from geodetic observations of interseismic coupling. *Nature Geoscience*,
 550 3(5), 363–369. doi: 10.1038/ngeo843
- 551 Kaneko, Y., Fialko, Y., Sandwell, D. T., Tong, X., & Furuya, M. (2013). Inter-
 552 seismic deformation and creep along the central section of the North Anatolo-
 553 lian Fault (Turkey): InSAR observations and implications for rate-and-state
 554 friction properties. *Journal of Geophysical Research: Solid Earth*, 118(1),
 555 316–331. doi: 10.1029/2012JB009661

- Kato, N., Satoh, T., Lei, X., Yamamoto, K., & Hirasawa, T. (1999). Effect of fault bend on the rupture propagation process of stick-slip. *Tectonophysics*, 310(1), 81–99. doi: 10.1016/S0040-1951(99)00149-3
- King, G., & Nabelek, J. (1985). Role of Fault Bends in the Initiation and Termination of Earthquake Rupture. *Science*, 228(4702), 984–987. doi: 10.1126/science.228.4702.984
- King, G. C. P. (1986). Speculations on the geometry of the initiation and termination processes of earthquake rupture and its relation to morphology and geological structure. *pure and applied geophysics*, 124(3), 567–585. doi: 10.1007/BF00877216
- Klinger, Y. (2010). Relation between continental strike-slip earthquake segmentation and thickness of the crust. *Journal of Geophysical Research: Solid Earth*, 115(B7). doi: 10.1029/2009JB006550
- Langer, L., Ragon, T., Sladen, A., & Tromp, J. (2020). Impact of topography on earthquake static slip estimates. *Tectonophysics*, 228566. doi: 10.1016/j.tecto.2020.228566
- Liang, C., & Fielding, E. J. (2017a). Interferometry With ALOS-2 Full-Aperture ScanSAR Data. *IEEE Transactions on Geoscience and Remote Sensing*, 55(5), 2739–2750. doi: 10.1109/TGRS.2017.2653190
- Liang, C., & Fielding, E. J. (2017b). Measuring Azimuth Deformation With L-Band ALOS-2 ScanSAR Interferometry. *IEEE Transactions on Geoscience and Remote Sensing*, 55(5), 2725–2738. doi: 10.1109/TGRS.2017.2653186
- Liu-Zeng, J., Klinger, Y., Xu, X., Lasserre, C., Chen, G., Chen, W., ... Zhang, B. (2007). Millennial Recurrence of Large Earthquakes on the Haiyuan Fault near Songshan, Gansu Province, China. *Bulletin of the Seismological Society of America*, 97(1B), 14–34. doi: 10.1785/0120050118
- Lohman, R. B., & Simons, M. (2005). Some thoughts on the use of InSAR data to constrain models of surface deformation: Noise structure and data down-sampling. *Geochemistry, Geophysics, Geosystems*, 6(1), Q01007. doi: 10.1029/2004GC000841
- Maden, N. (2012). One-Dimensional Thermal Modeling of the Eastern Pontides Orogenic Belt (NE Turkey). *Pure and Applied Geophysics*, 169(1), 235–248. doi: 10.1007/s00024-011-0296-0

- 589 Mai, P. M., Schorlemmer, D., Page, M., Ampuero, J.-P., Asano, K., Causse, M., ...
 590 Zielke, O. (2016). The Earthquake-Source Inversion Validation (SIV) Project.
 591 *Seismological Research Letters*. doi: 10.1785/0220150231
- 592 McClusky, S., Balassanian, S., Barka, A., Demir, C., Ergintav, S., Georgiev, I., ...
 593 Veis, G. (2000). Global Positioning System constraints on plate kinematics and
 594 dynamics in the eastern Mediterranean and Caucasus. *Journal of Geophysical
 595 Research: Solid Earth*, 105(B3), 5695–5719. doi: 10.1029/1999JB900351
- 596 McKenzie, D. (1972). Active Tectonics of the Mediterranean Region. *Geophysical
 597 Journal International*, 30(2), 109–185. doi: 10.1111/j.1365-246X.1972.tb02351
 598 .x
- 599 Mckenzie, D. P. (1970). Plate Tectonics of the Mediterranean Region. *Nature*,
 600 226(5242), 239–243. doi: 10.1038/226239a0
- 601 Melgar, D., Ganas, A., Taymaz, T., Valkaniotis, S., Crowell, B. W., Kapetani-
 602 dis, V., ... Öcalan, T. (2020). Rupture kinematics of January 24, 2020
 603 Mw 6.7 Doğanyol-Sivrice, Turkey earthquake on the East Anatolian Fault
 604 zone imaged by space geodesy. *Geophysical Journal International*. doi:
 605 10.1093/gji/ggaa345
- 606 Minson, S. E., Simons, M., & Beck, J. L. (2013). Bayesian inversion for finite fault
 607 earthquake source models I – theory and algorithm. *Geophysical Journal Inter-
 608 national*, 194(3), 1701–1726. doi: 10.1093/gji/ggt180
- 609 Minson, S. E., Simons, M., Beck, J. L., Ortega, F., Jiang, J., Owen, S. E., ...
 610 Sladen, A. (2014). Bayesian inversion for finite fault earthquake source mod-
 611 els – II: The 2011 great Tohoku-oki, Japan earthquake. *Geophysical Journal
 612 International*, 198(2), 922–940. doi: 10.1093/gji/ggu170
- 613 NEIC. (2020). *NEIC Earthquake catalogue*. National Earthquake Information Cen-
 614 tre, On-line Bulletin,. <https://earthquake.usgs.gov/earthquakes/search/>.
- 615 Ozer, C., Ozyazicioglu, M., Gok, E., & Polat, O. (2019). Imaging the Crustal
 616 Structure Throughout the East Anatolian Fault Zone, Turkey, by Local Earth-
 617 quake Tomography. *Pure and Applied Geophysics*, 176(6), 2235–2261. doi:
 618 10.1007/s00024-018-2076-6
- 619 Perfettini, H., Avouac, J.-P., Tavera, H., Kositsky, A., Nocquet, J.-M., Bondoux, F.,
 620 ... Soler, P. (2010). Seismic and aseismic slip on the Central Peru megathrust.
 621 *Nature*, 465(7294), 78–81.

- 622 Perrin, C., Manighetti, I., & Gaudemer, Y. (2016). Off-fault tip splay net-
 623 works: A genetic and generic property of faults indicative of their long-
 624 term propagation. *Comptes Rendus Geoscience*, *348*(1), 52–60. doi:
 625 10.1016/j.crte.2015.05.002
- 626 Persson, P.-O., & Strang, G. (2004). A Simple Mesh Generator in MATLAB. *SIAM*
 627 *Review*, *46*(2), 329–345. doi: 10.1137/S0036144503429121
- 628 Pousse-Beltran, L., Nissen, E., Bergman, E. A., Cambaz, M. D., Gaudreau, É.,
 629 Karasözen, E., & Tan, F. (2020). The 2020 Mw 6.8 Elazığ (Turkey) Earth-
 630 quake Reveals Rupture Behavior of the East Anatolian Fault. *Geophysical*
 631 *Research Letters*, *47*(13), e2020GL088136. doi: 10.1029/2020GL088136
- 632 Ragon, T., Sladen, A., Bletery, Q., Vergnolle, M., Cavalié, O., Avallone, A., ... De-
 633 louis, B. (2019). Joint Inversion of Coseismic and Early Postseismic Slip to
 634 Optimize the Information Content in Geodetic Data: Application to the 2009
 635 Mw6.3 L'Aquila Earthquake, Central Italy. *Journal of Geophysical Research:*
 636 *Solid Earth*, *124*(10), 10522–10543. doi: 10.1029/2018JB017053
- 637 Ragon, T., Sladen, A., & Simons, M. (2018). Accounting for uncertain fault
 638 geometry in earthquake source inversions – I: Theory and simplified ap-
 639 plication. *Geophysical Journal International*, *214*(2), 1174–1190. doi:
 640 10.1093/gji/ggy187
- 641 Ragon, T., Sladen, A., & Simons, M. (2019). Accounting for uncertain fault geom-
 642 etry in earthquake source inversions – II: Application to the Mw 6.2 Amatrice
 643 earthquake, central Italy. *Geophysical Journal International*, *218*(1), 689–707.
 644 doi: 10.1093/gji/ggz180
- 645 Razafindrakoto, H. N. T., & Mai, P. M. (2014). Uncertainty in Earthquake Source
 646 Imaging Due to Variations in Source Time Function and Earth Structure. *Bul-
 647 letin of the Seismological Society of America*, *104*(2), 855–874. doi: 10.1785/
 648 0120130195
- 649 Reilinger, R., McClusky, S., Vernant, P., Lawrence, S., Ergintav, S., Cakmak, R., ...
 650 Karam, G. (2006). GPS constraints on continental deformation in the Africa-
 651 Arabia-Eurasia continental collision zone and implications for the dynamics of
 652 plate interactions. *Journal of Geophysical Research: Solid Earth*, *111*(B5). doi:
 653 10.1029/2005JB004051

- 654 Rosen, P. A. G. (2012). The InSAR Scientific Computing Environment. In *9th Eu-*
 655 *ropean Conference on Synthetic Aperture Radar*. Nuremberg, Germany.
- 656 Schmittbuhl, J., Karabulut, H., Lengliné, O., & Bouchon, M. (2016). Long-lasting
 657 seismic repeaters in the Central Basin of the Main Marmara Fault. *Geophysical*
 658 *Research Letters*, 43(18), 9527–9534. doi: 10.1002/2016GL070505
- 659 Şengör, A., Tüysüz, O., İmren, C., Sakınç, M., Eyidoğan, H., Görür, N., ...
 660 Rangin, C. (2005). The North Anatolian Fault: A New Look. *Annual*
 661 *Review of Earth and Planetary Sciences*, 33(1), 37–112. doi: 10.1146/annurev.earth.32.101802.120415
- 662 Stein, R. S., Barka, A. A., & Dieterich, J. H. (1997). Progressive failure on the
 663 North Anatolian fault since 1939 by earthquake stress triggering. *Geophysical*
 664 *Journal International*, 128(3), 594–604. doi: 10.1111/j.1365-246X.1997.tb05321
 665 .x
- 666 Tan, O., Pabuçcu, Z., Tapirdamaz, M. C., İnan, S., Ergintav, S., Eyidoğan, H., ...
 667 Kuluöztürk, F. (2011). Aftershock study and seismotectonic implications
 668 of the 8 March 2010 Kovancılar (Elazığ, Turkey) earthquake (MW = 6.1).
 669 *Geophysical Research Letters*, 38(11). doi: 10.1029/2011GL047702
- 670 Tarantola, A. (2005). *Inverse Problem Theory and Methods for Model Parameter Es-*
 671 *timation*. Society for Industrial and Applied Mathematics.
- 672 Tatar, O., Sözbilir, H., Koçbulut, F., Bozkurt, E., Aksoy, E., Eski, S., ... Metin, Y.
 673 (2020). Surface deformations of 24 January 2020 Sivrice (Elazığ)–Doğanyol
 674 (Malatya) earthquake ($M_w = 6.8$) along the Pütürge segment of the East Ana-
 675 tolian Fault Zone and its comparison with Turkey's 100-year-surface ruptures.
 676 *Mediterranean Geoscience Reviews*. doi: 10.1007/s42990-020-00037-2
- 677 Twardzik, C., Vergnolle, M., Sladen, A., & Avallone, A. (2019). Unravelling the con-
 678 tribution of early postseismic deformation using sub-daily GNSS positioning
 679 —. *Scientific Reports*, 9(1), 1775. doi: 10.1038/s41598-019-39038-z
- 680 Vallée, M., & Douet, V. (2016). A new database of source time functions (STFs) ex-
 681 tracted from the SCARDEC method. *Physics of the Earth and Planetary Inte-*
 682 *riors*, 257, 149–157. doi: 10.1016/j.pepi.2016.05.012
- 683 Walters, R. J., Holley, R. J., Parsons, B., & Wright, T. J. (2011). Interseismic strain
 684 accumulation across the North Anatolian Fault from Envisat InSAR measure-
 685 ments. *Geophysical Research Letters*, 38(5). doi: 10.1029/2010GL046443

- 687 Wells, D. L., & Coppersmith, K. J. (1994). New empirical relationships among mag-
688 nitude, rupture length, rupture width, rupture area, and surface displacement.
689 *Bulletin of the Seismological Society of America*, 84(4), 974–1002.
- 690 Wesnousky, S. G. (2006). Predicting the endpoints of earthquake ruptures. *Nature*,
691 444(7117), 358–360. doi: 10.1038/nature05275
- 692 Wessel, P., Luis, J. F., Uieda, L., Scharroo, R., Wobbe, F., Smith, W. H. F., & Tian,
693 D. (2019). The Generic Mapping Tools Version 6. *Geochemistry, Geophysics,
Geosystems*, n/a(n/a). doi: 10.1029/2019GC008515
- 694 Wright, T., Parsons, B., & Fielding, E. (2001). Measurement of interseismic
695 strain accumulation across the North Anatolian Fault by satellite radar
696 interferometry. *Geophysical Research Letters*, 28(10), 2117–2120. doi:
697 10.1029/2000GL012850
- 698 Xu, X., Tong, X., Sandwell, D. T., Milliner, C. W. D., Dolan, J. F., Hollingsworth,
699 J., ... Ayoub, F. (2016). Refining the shallow slip deficit. *Geophysical Journal
700 International*, 204(3), 1867–1886. doi: 10.1093/gji/ggv563
- 701 Yagi, Y., & Fukahata, Y. (2008). Importance of covariance components in inver-
702 sion analyses of densely sampled observed data: An application to waveform
703 data inversion for seismic source processes. *Geophysical Journal International*,
704 175(1), 215–221. doi: 10.1111/j.1365-246X.2008.03884.x
- 705 Yilmaz, H., Over, S., & Ozden, S. (2006). Kinematics of the East Anatolian
706 Fault Zone between Turkoglu (Kahramanmaraş) and Celikhan (Adiya-
707 man), eastern Turkey. *Earth, Planets and Space*, 58(11), 1463–1473. doi:
708 10.1186/BF03352645
- 709 Zhu, L., & Rivera, L. A. (2002). A note on the dynamic and static displacements
710 from a point source in multilayered media. *Geophysical Journal International*,
711 148(3), 619–627. doi: 10.1046/j.1365-246X.2002.01610.x
- 712

Figure 1.

Accepted Article

This article is protected by copyright. All rights reserved.

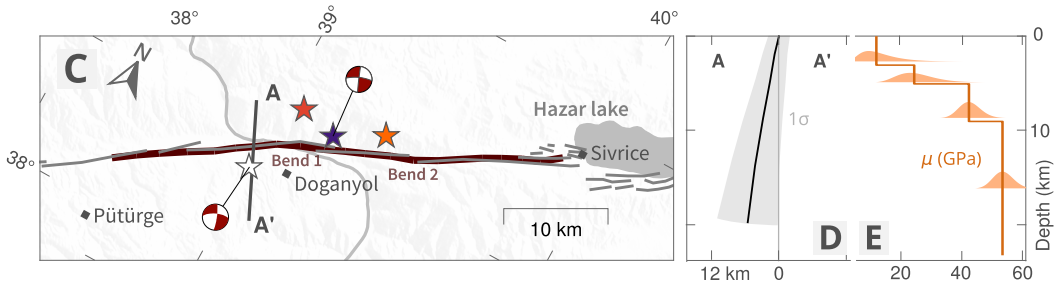
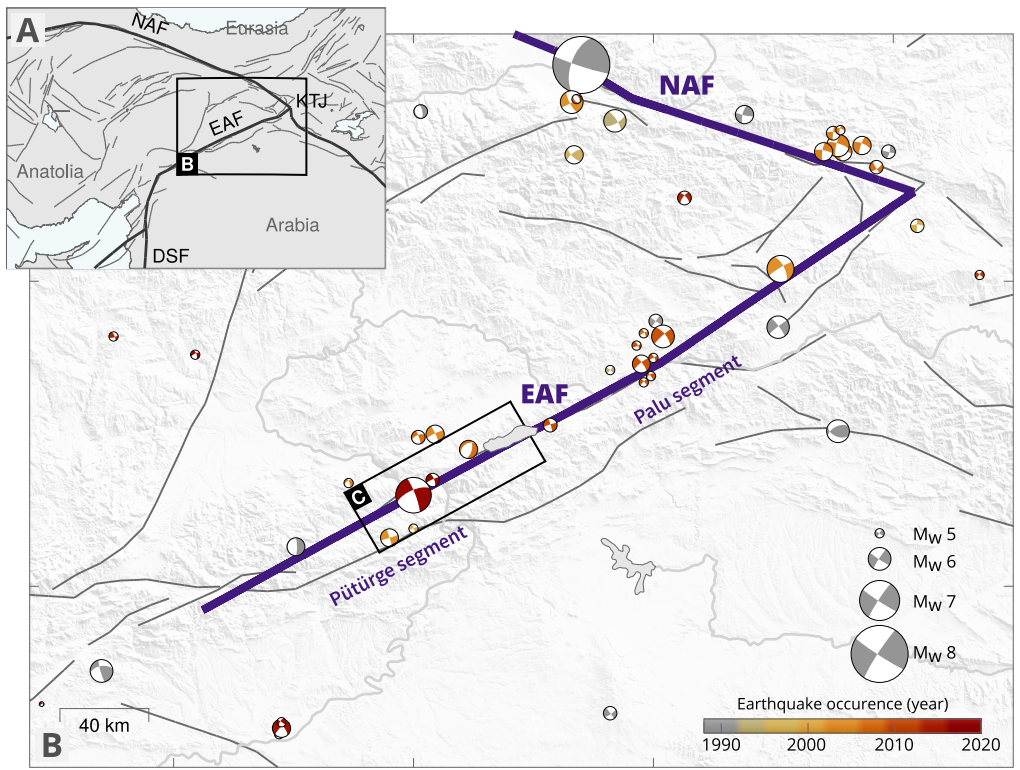
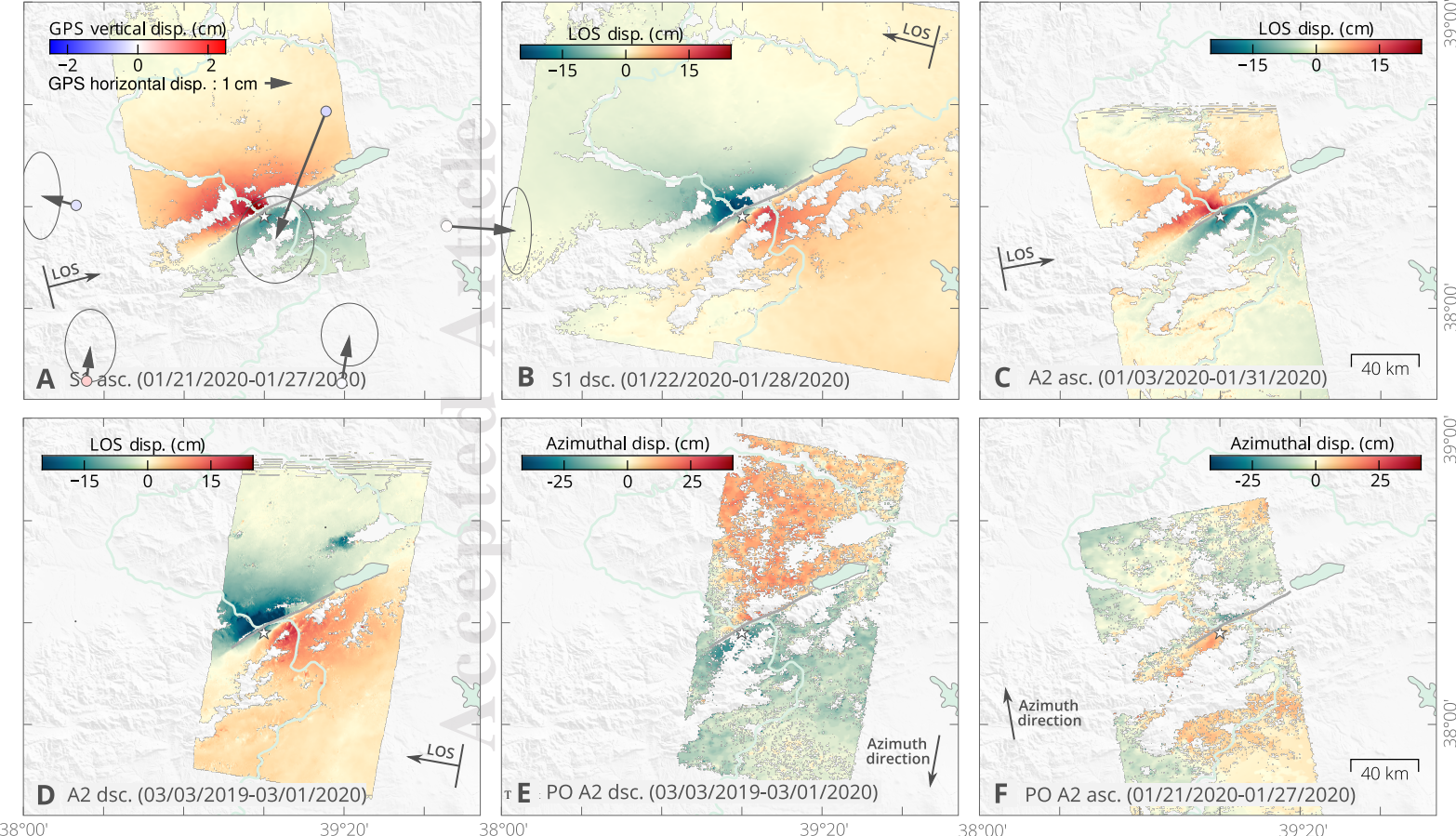


Figure 2.

Accepted Article

This article is protected by copyright. All rights reserved.



Accepted Article

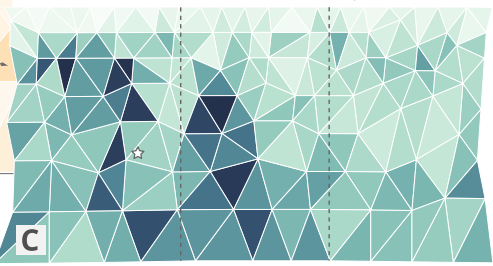
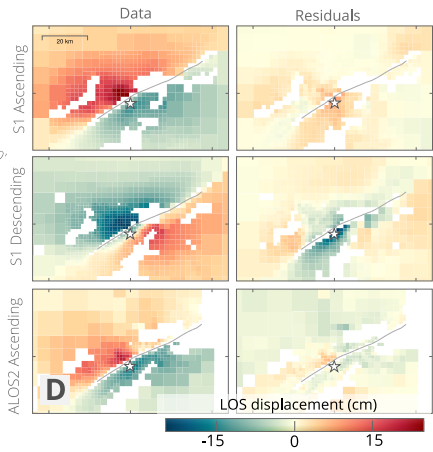
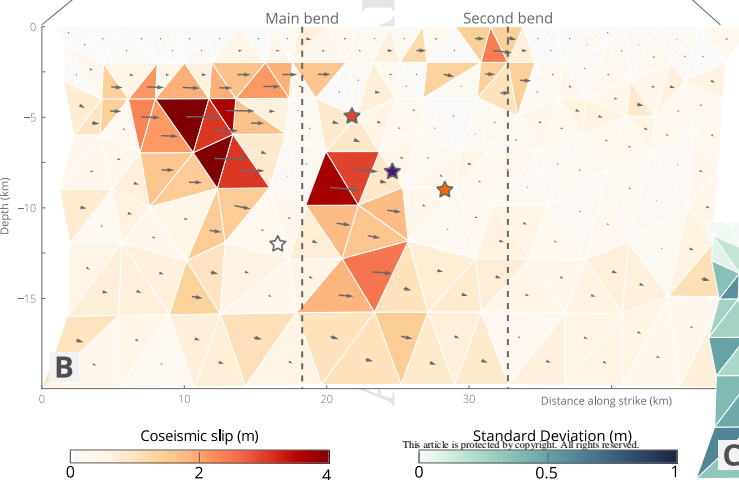
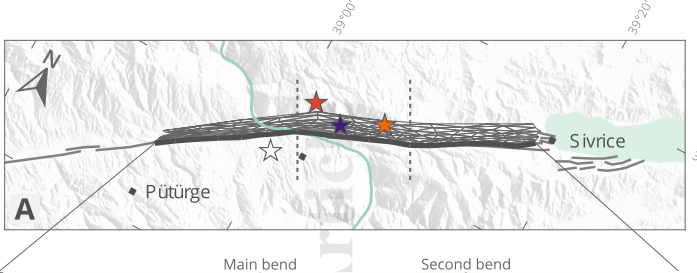


Figure 4.

Accepted Article

This article is protected by copyright. All rights reserved.

